photonics

MDPI

Review

Semiconductor Nanomembrane-Based Light-Emitting and Photodetecting Devices

Dong Liu [1], Weidong Zhou [2] and Zhenqiang Ma [1,*]

[1] Department of Electrical and Computer Engineering, University of Wisconsin-Madison, Madison, WI 53706, USA; dliu93@wisc.edu

[2] Department of Electrical Engineering, University of Texas at Arlington, Arlington, TX 76019, USA; wzhou@uta.edu

* Correspondence: mazq@engr.wisc.edu; Tel.: +1-608-261-1095

Received: 1 June 2016; Accepted: 14 June 2016; Published: 17 June 2016

Abstract: Heterogeneous integration between silicon (Si), III-V group material and Germanium (Ge) is highly desirable to achieve monolithic photonic circuits. Transfer-printing and stacking between different semiconductor nanomembranes (NMs) enables more versatile combinations to realize high-performance light-emitting and photodetecting devices. In this paper, lasers, including vertical and edge-emitting structures, flexible light-emitting diode, photodetectors at visible and infrared wavelengths, as well as flexible photodetectors, are reviewed to demonstrate that the transfer-printed semiconductor nanomembrane stacked layers have a large variety of applications in integrated optoelectronic systems.

Keywords: transfer printing; semiconductor nanomembrane; light-emitting diode; photodetectors; flexible optoelectronics; silicon photonics

1. Introduction

The applications of semiconductor nanomembrane (NM) transfer technology both in electronic and photonics have attracted intensive attention and research interests [1–24]. The basic concept is instead of using the whole bulk material grown from substrate up to the functional layer, the top functional membrane layer is released from its original substrate and transfer printed on a new host. Pioneered by Rogers *et al.*, a polydimethylsiloxane (PDMS) stamp-assisted transfer printing process has been used to transfer a variety of crystalline semiconductor NMs on different foreign host substrates. This heterogeneous materials stack could be integrated with Si and flexible substrate applications [25–33].

The two most attractive characteristics of this semiconductor NM are: (1) flexibility, as the semiconductor material is stretchable or bendable when in the form of thin layer (nanometers scale), which is a highly desired mechanical property for flexible optoelectronic devices; (2) transferability to a variety of foreign substrates, without the limitation by different materials' growths condition and lattice mismatch; heterogeneous integration could be formed between various combinations of materials to serve a multi-functional and versatile purpose. Up to now, semiconductor NMs have been successfully transferred onto numerous kinds of substrates, including glass [34–36], plastics [24–27], biodegradable nanofibril paper [37], *etc.*

The transfer printing process basically consists of two main process: one is the release of crystalline semiconductor NMs from the original growth substrate using selective etching; the other is transfer printing onto the targeted substrate, as shown in Figure 1. During the selective etching step in Figure 1a–c, the sacrificial layer underneath the desired NMs or strips is etched away, and still in the etchant environment, the NMs fall on and bond with the substrate by a weak van der Waals force (Figure 1d). Then, the NMs are ready to be picked up, and there are generally three approaches to

transfer the NMs to a new host: (1) direct flip transfer; (2) stamp-assisted transfer; and (3) transfer printing without an adhesive layer, depicted in Figure 1e–g, respectively. For the former two methods, an adhesive layer, such as SU-8, is necessary for the foreign substrate to be coated to enhance the bonding strength. While for the one called dry transfer printing without an adhesive layer, kinetically-controlled adhesion of the elastomeric stamp is employed to leave the NMs on the new host [14–17]. The basic principle is fast peeling speed during pick-up and slow for releasing NMs.

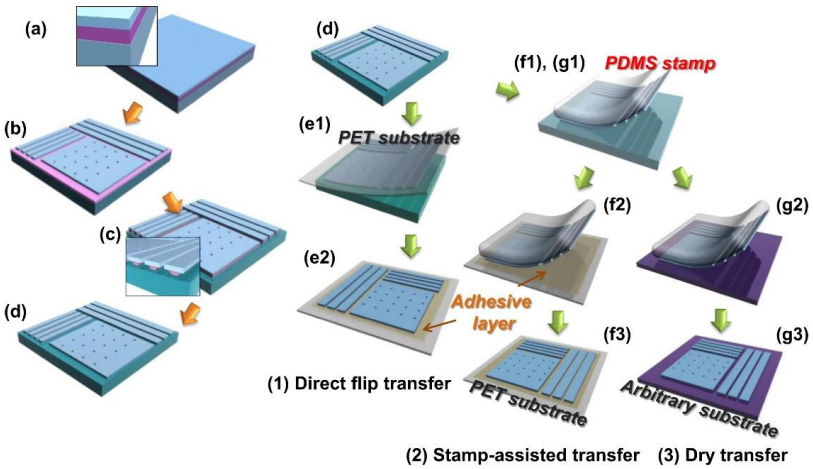

Figure 1. Generic process of a transfer printing: (**a**,**b**) make a pattern on an silicon on insulator (SOI) wafer; (**c**) immerse in the etchant for the undercut; (**d**) the membrane layer gently falls down after the buried oxide layer is completely removed; (**e1**) the adhesive layer-coated plastic substrate is flipped and the membranes picked; (**e2**) completion of the direct flip transfer; (**f1**) pick up the membranes by the elastomeric stamp; (**f2**) transfer printing on the adhesive layer-coated flexible substrate; (**f3**) completion of the stamp-assisted transfer; (**g1**) pick up the membranes with fast peeling speed; (**g2**) release the membrane with slow peeling speed; (**g3**) application of an additional annealing procedure to enhance the bonding force (reprinted from [18]).

In recent years, the impressive progress of NM transfer and stacked NMs in photonic applications has been implemented; one main research focus is integrating III-V material or efficient light-absorbing material onto silicon substrate for silicon photonics applications, including a vertical cavity laser with two Si photonic crystal (PC) mirrors [12], first-order diffraction-based surface emitting lasers with a Si PC pattern [30], an edge-emitting laser on Si substrate [38], multi-color photodetectors [39] and a cavity-enhanced Ge photodetector on a silicon on insulator (SOI) substrate [40]. The other is to take advantage of the flexible mechanical property to realize bendable phototransistors and photodetectors [25,41–43] and light-emitting diodes (LEDs) [44] by transfer printing a very thin membrane layer onto a plastic substrate.

2. Semiconductor NM-Based Light-Emitting Devices

Heterogeneous integration between light-emitting materials (III-V group) and other substrates (Si or flexible substrate) is highly demanded in applications, such as silicon photonics and flexible optoelectronic devices. Compared to wafer-bonding approaches, transfer printing is insensitive to the wafer-size mismatch and more efficient by substrate reuse [14]. Moreover, the developments in transfer printing techniques have enabled a clean and atomically-smooth interface after the transfer process, which is critical to reduce scattering loss when light is propagating along or through the interface.

In the section, three types of lasers, including vertical and edge-emitting structures based on NMs transfer printing, are reviewed from both fabrication and device performance perspectives. Furthermore, a GaN blue LED on a bendable substrate is also brought into discussion as a representative of the flexible light-emitting applications.

2.1. Lasers

2.1.1. Silicon-Based Vertical-Cavity Surface-Emitting Lasers

The laser source has been one of the most challenging topics on the path to achieve an integrated silicon photonics platform. Due to the indirect bandgap, silicon has to be heterogeneously integrated with compound semiconductor materials. Promising approaches, including direct growth of III-V material on silicon substrate [45] and wafer boding between III-V and silicon [46,47], are demonstrated and reported. The lattice mismatches and different material growth conditions stand out as big issues for high quality growth, as it is still limited to quantum dot or quantum wire applications. Comparatively, bonding provides a more practical way to bring the III-V and silicon together, which has been employed by edge-emitting laser designs [47]. However, the wafer size mismatch and III-V substrate removal make inefficient use of material and consequently render this approach costly.

Researcher Yang *et al.* reported nanomembrane transfer printing-based vertical-cavity surface-emitting lasers (VCSELs) on a silicon platform, which not only enjoys similar benefits as the bonding process in terms of mismatch compatibility, but also makes more efficient use of the III-V material by recycling the III-V substrate. Figure 2 shows the schematic and SEM images of the vertical laser cavity, which consists of InGaAsP quantum wells as gain region and two Fano resonance membrane reflectors (MRs) made of single crystal silicon NMs. The device fabrication process requires two-step transfer-printing, firstly the III-V QW NM released from its original substrate is transferred on a patterned SOI as the bottom mirror, and then, the top Si NM mirror with the glass substrate holder is stacked on top of quantum wells (QWs). Between Si and QWs, there is hundreds of nanometers thick SiO_2 to achieve 6% field intensity confinement in the QWs region. Thus, a vertical cavity with a III-V QW region sandwiched by two PC mirrors is formed.

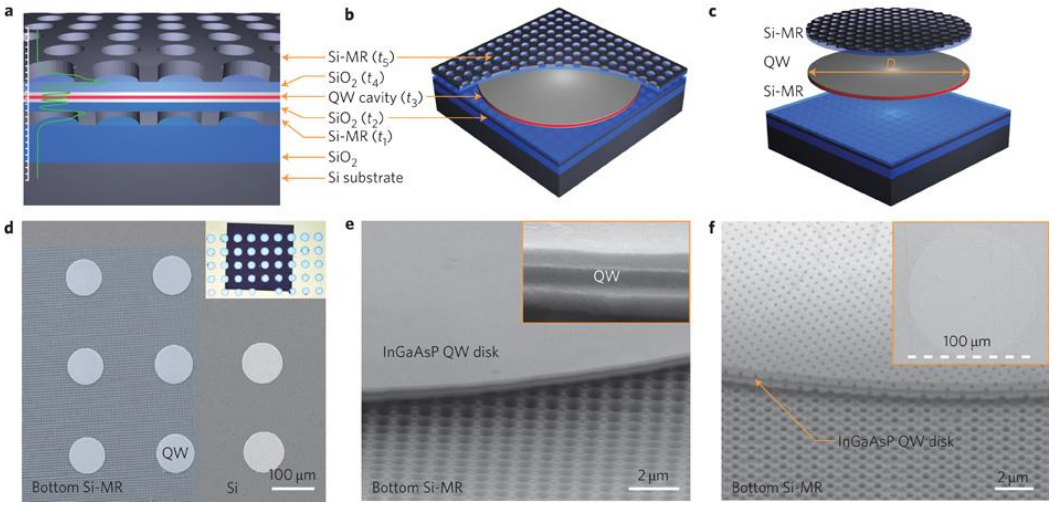

Figure 2. Vertical-cavity surface-emitting lasers (VCSEL) on silicon. (**a**) Schematic of a lasing cavity that consists of five layers (t1–t5), with a total thickness of 1–2 wavelengths. An InGaAsP quantum well (QW) is sandwiched between two single-layer Si-MRs. Also shown is a simulated electrical field distribution in the cavity for a lasing mode at 1527 nm, with a confinement factor of 6%. (**b**) A cutout view of the complete MR-VCSEL. (**c**) Illustration of the multilayer printing process for the formation of an MR-VCSEL (top Si-MR/quantum well/bottom Si-MR). The diameter of the active area is D. (**d**) SEM image of InGaAsP quantum well disks/mesas transferred onto a bottom Si-MR. Inset: optical image, showing a central dark region representing the 1×1 mm^2 bottom membrane reflector. (**e**) Zoom-in view of one InGaAsP quantum well disk on the bottom Si-MR. Inset: quantum well heterostructure, (**f**) SEM image of a complete MR-VCSEL, showing an InGaAsP quantum well disk sandwiched between top and bottom Si-MRs. Inset: SEM top view of an InGaAsP quantum well disk underneath a large top Si-MR layer (reprinted from [12]).

By carefully adjusting the silicon photonic crystal Fano resonance peak spectrum, single mode operation is achieved with a 532-nm optical pump source. The spectrum linewidth is 0.6 nm when operating above a threshold pump power of 8 mW, which is about 0.32 kW· cm^{-2} for low temperature (LT) (50 K) measurement. As for room temperature (RT), the threshold is increased two times, and the lasing linewidth nearly remains unchanged, as shown in Figure 3a. Furthermore, the wavelength tunability is demonstrated by different PC lattice designs to shift the reflection spectrum towards the target wavelength (Figure 3b).

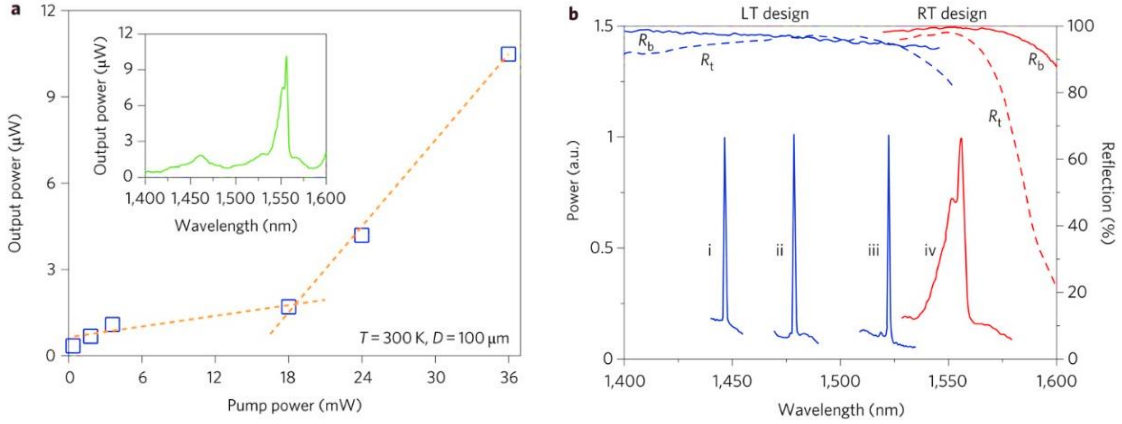

Figure 3. (**a**) Laser Light-light (L-L) curve at room temperature for the RT design of the MR-VCSEL device. Inset: measured spectral output above the threshold at a pump power of 36 mW, (**b**) Measured MR-VCSEL spectral outputs at different temperatures for both LT and RT designs: (i) T = 10 K; (ii) T = 50 K; (iii) T = 120 K; (iv) T = 300 K. Portions of measured top (R_t, dash lines) and bottom (R_b, solid lines) reflection spectra are also shown for both LT and RT designs (reprinted from [12]).

This provides a promising and practical approach to achieve full wafer-scale multi-wavelength laser sources for silicon photonics. It is also worth noting that the whole cavity thickness is only 2.4 μm and viable if transferred onto flexible plastic substrate, expanding its application in flexible optoelectronics and biophotonics.

2.1.2. Photonic Crystal Surface-Emitting Laser

The photonic crystal surface-emitting laser (PCSEL) has drawn much attention due to the advantages, including single mode, both longitudinally and transversely, low threshold, high power and beam control [48–51]. The band edge effect is used to achieve zero group velocity, which theoretically has infinite gain at the specific wavelength; therefore, one lasing mode is selected dominantly over others. Then, the in-plane transmitting light waves are diffracted upwards out of the cavity by the photonic crystal due to first order Bragg diffraction [48,49]. The critical requisite to form a PCSEL is that the light propagating in the cavity should, on the one hand, couple adequately with the PC cavity to fully make use of the band edge effect and, on the other hand, have a high confinement factor in the active region. Thus, it requires the appropriate distance proximity between the quantum well layer and the PC layer. For homogeneous material growth, this structure is realized by PC pattern definition etching and the QW regrowth process to ensure adequate feedback from different PC units by mode evanescent coupling with the PC cavity [49].

Comparatively, NM transfer printing provides a simpler and lower-cost approach to bring the PC structure and gain medium together. Deyin *et al.* demonstrated a novel approach to realize large-area PCSEL based on a heterogeneously-integrated III-V membrane transfer-printed onto a patterned silicon PC structure with SOI substrate. Figure 4a shows the schematic structure of the transferred InGaAsP multi-quantum well (MQW) layer on top of patterned Si PC layer. To compare the effect of different coupling strengths on lasing performance, two devices with different spacing between

MQWs and Si-PC (0 and 130 nm) are fabricated, named PCSEL-I and PCSEL-II. The SEM image of the transferred membrane on Si, the patterned Si cavity and cross-sectional view of the PCSEL-II are also shown respectively as in Figure 4b–d.

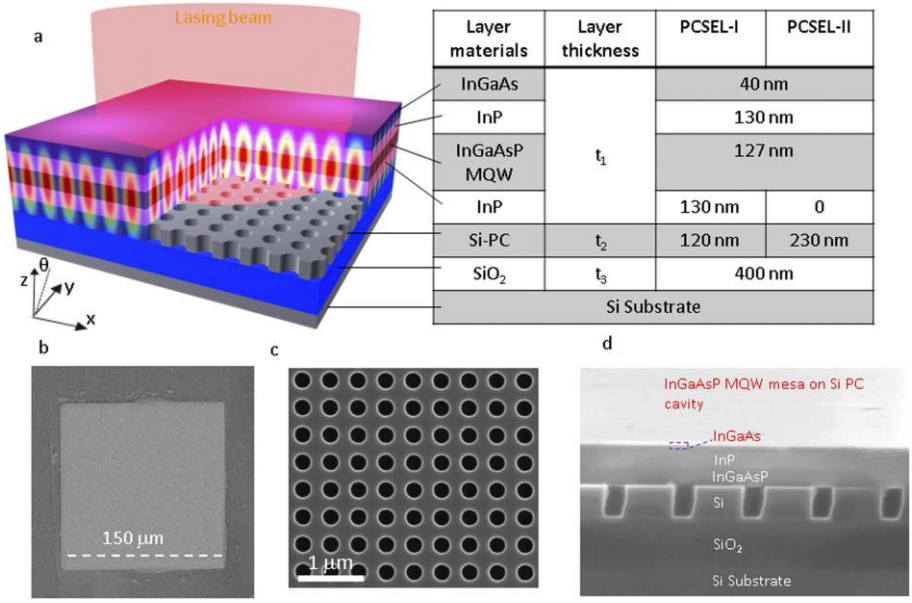

Figure 4. Photonic crystal surface-emitting laser (PCSEL) on silicon. (**a**) Schematic of the hybrid III-V/Si PCSEL cavity on Si substrate, which consists of the III-V active multi-quantum well (MQW) structure and the Si-PC cavity. Also shown is the simulated electrical field distribution in the cavity for a lasing mode at 1424 nm. (**b**) An SEM image of the InGaAsP QW disk/mesa transferred onto a Si-PC. (**c**) Zoomed-in view of the defect-free Si-PC cavity. (**d**) Cross-sectional view of the cavity (reprinted from [30]).

Photoluminescences (PLs) are measured for the two types of designs, and temperature-dependent characteristics are compared in terms of lasing power, linewidth, optical pump threshold, side mode suppression ratio (SMSR) and the output beam polarization property. The results as in Figure 5 show that type I and II have different best-performance temperature at 25 K and 180 K, respectively. Device I has a lower threshold pump power of 6 mW (about 0.1 kW/cm^2), compared to Device II with 25 mW (Figure 5a,d); while on the other hand, the PCSEL-II outperforms PCSEL-I, with respect to lasing spectrum linewidth and peak power, derived from Figure 5b,e.

The correlation between the lasing spectrum and simulated band diagram of the PC cavity is found, which reveals the underlying physical explanations regarding the differences between the two designs. As more light is confined in Si for PCSEL-II, which has a thicker Si slab and a direct contact between QWs and Si, the effective mode refractive index (n) for PCSEL-II is higher than PCSEL-I, since Si has higher n than the InP and InGaAsP material. As a result, the lasing modes' wavelengths for PCSEL-II (1505 nm) are red shifted compared to PCSEL-I (1425 nm). Thus, to obtain more gain, higher temperature (180 K) is favored to red shift the QW PL spectrum to match the lasing mode wavelength. As for better performances in the narrow linewidth (0.6 nm) and lasing peak power of PCSEL-II, it is also attributed to stronger light confinement in PC Si, which induces a stronger feedback mechanism to achieve lasing. Both devices show one dominant polarization direction, shown as in Figure 5c,f. Comparing the two different structures and lasing characteristics, it is speculated that stronger coupling strength between QWs and the PC cavity could further improve the lasing properties, including peak power and linewidth.

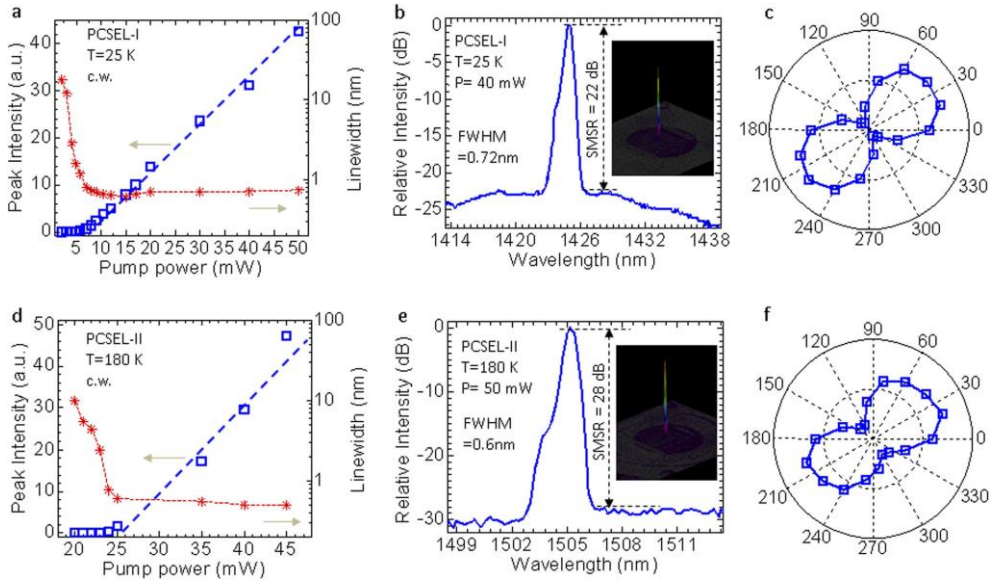

Figure 5. Lasing characteristics. (**a**) Lasing power and linewidth versus input pump power for PCSEL-I at T = 25 K. (**b**) Lasing spectral output (plotted in semi-log scale) above the pumping threshold (Inset: far-field image). (**c**) Measured polarization properties above threshold at λ = 1424 nm. (**d**) Lasing power and linewidth versus input pump power for PCSEL-II at T = 180 K. (**e**) Lasing spectral output (plotted in semi-log scale) above the pumping threshold (Inset: far-field image). (**f**) Measured polarization properties above threshold at λ = 1505 nm.

With the membrane transfer printing technique, the heterogeneously-integrated band edge surface-emitting laser provides a new promising approach to realize a large-scale single-mode laser source for silicon-based photonic platform.

2.1.3. Edge-Emitting Lasers

Transfer printing is also applicable for III-V edge-emitting lasers based on silicon substrate [38]. John *et al.* demonstrated a wafer-scale integration of AlGaAs lasers on silicon using transfer printing of epitaxial layers, as shown in Figure 6. The two AlInGaAs QWs are grown on GaAs substrate with a 1 μm-thick $Al_{0.95}Ga_{0.05}As$ sacrificial layer, which is etched away later to release the NM from the native substrate. To form the Fabry-Perot (FP) cavity after being transfer printed on silicon substrate, the mirror facets are etched using SiO_2 by deep anisotropic inductively-coupled plasma (ICP), which is independent of crystal orientation. The ridge waveguide is 3 μm wide and 370 μm long with single transverse mode. P- and n-type metal contacts are formed on top of the waveguide and the etched recess n-doping AlGaAs layer at one side of the waveguide, as shown in Figure 6b.

The electrical pumped edge-emitting lasers show comparable performances with the same sized cleaved facet lasers on the original GaAs substrate under the continuous-wave current operation condition, shown as in Figure 7a. At room temperature, the threshold is 17 mA and 14 mA for silicon and GaAs substrate, respectively. The decrease in optical power collected from facet may result from the inefficient output light coupling, the p-type contact not fully covering the ridge near the facet ends and increased n side lateral resistance with the thinner n-AlGaAs layer. Typical FP modes (Figure 7b) are observed with about a 0.2-nm spacing between adjacent longitudinal modes, which corresponds to the waveguide length of 370 μm. The small signal measurement shows up to a 3-GHz direct modulation bandwidth (Figure 7c), with no obvious degradation compared to the one on the native substrate. Furthermore, the light/current (L-I) characteristics are measured under different temperatures for a 6 μm-wide ridge (Figure 7d); at a 125-mA current injection, the edge emitting laser has a total power of 33 mW with a wall-plug efficiency of 13%.

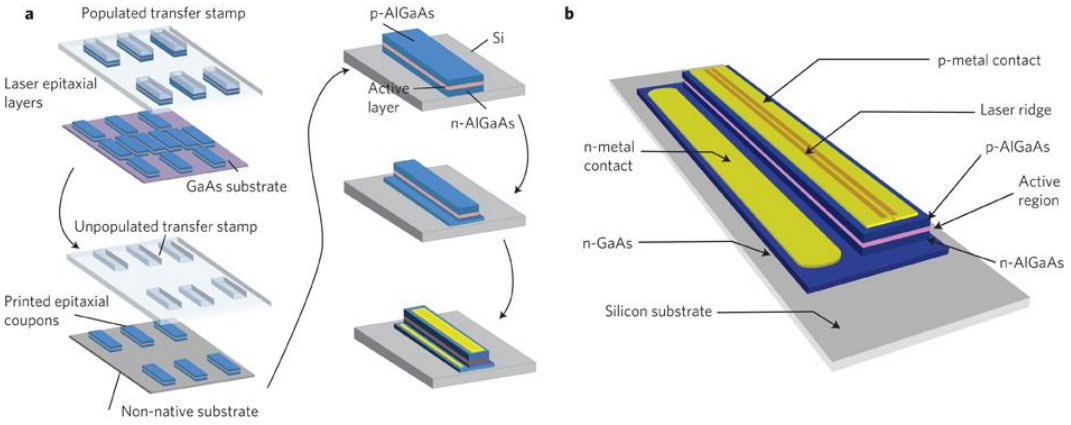

Figure 6. (**a**) Schematic of the transfer of unprocessed coupons of epitaxial material from a native III-V wafer (containing the desired layer structure) to the host substrate. The laser devices are fabricated in parallel on the host substrate using lithographically-defined etched facets to align to the underlying alignment marks. (**b**) Schematic of a laser on the silicon substrate (reprinted from [38]).

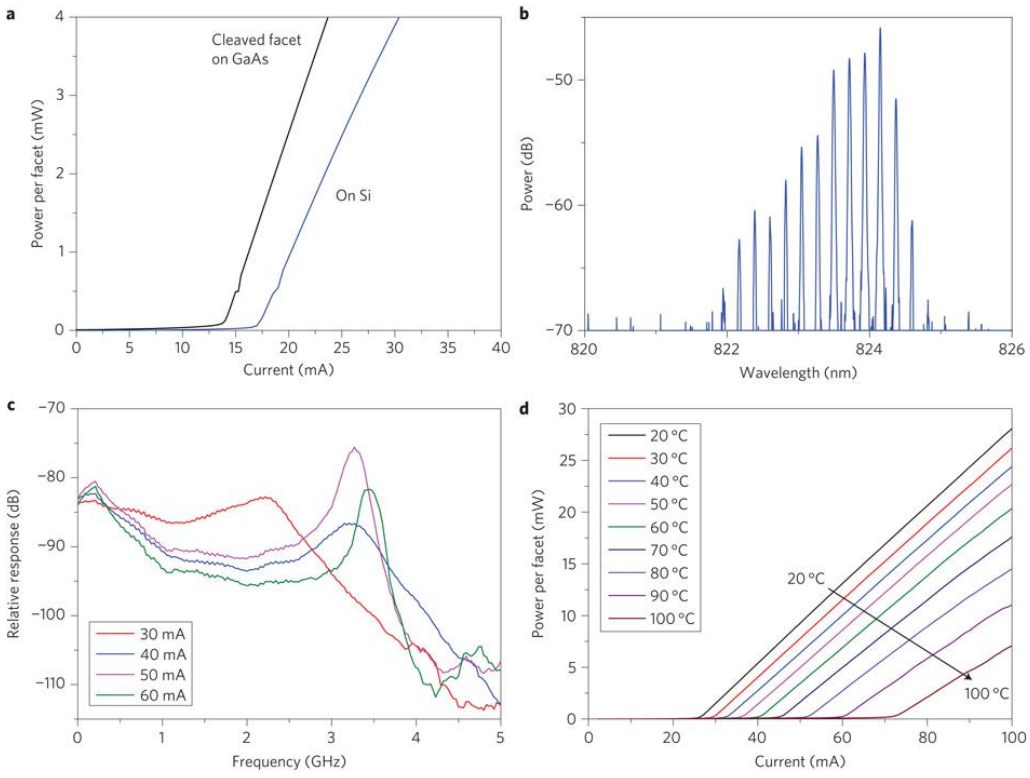

Figure 7. (**a**) Optical power as a function of current from a 3 μm-wide ridge, 370 μm-long laser fabricated on silicon, compared to a similar device fabricated using a standard cleaved facet on native GaAs substrate. (**b**) Spectrum of the laser showing the multiple longitudinal mode emission. (**c**) Small signal modulation response of the laser on silicon as a function of operating current from 30–60 mA. (**d**) Temperature dependence of the output power as a function of current from a 6 μm-wide ridge, 370 μm-long laser fabricated on silicon (reprinted from [38]).

In this work, the transfer printing method has been successfully proven to be applicable in the wafer-scale integration of III-V active material onto non-native substrates in silicon photonics and flexible optoelectronics.

2.2. Flexible Light-Emitting Diode

Recently, we have reported transfer printing-based flexible blue LEDs by transferring the GaN membrane on a flexible plastic substrate by transfer printing [44]. Due to the lattice mismatch, the GaN buffer layer before QW growth on sapphire substrates needs to be at least a few microns thick in order to achieve an acceptable GaN crystal quality. As a result, built-in stress would induce fractures when laser lift-off (LLO) is applied to separate the GaN structure from the sapphire substrate if not tightly bonded to a mechanically-compatible substrate. It is proposed in this report that elastic and soft PDMS is employed to strongly bond the GaN layer during the LLO process, and then, the stress is fully relaxed after being transferred onto a polyethylene terephthalate (PET) stretchable substrate. Figure 8 shows the main process flows and LED chip image on PET.

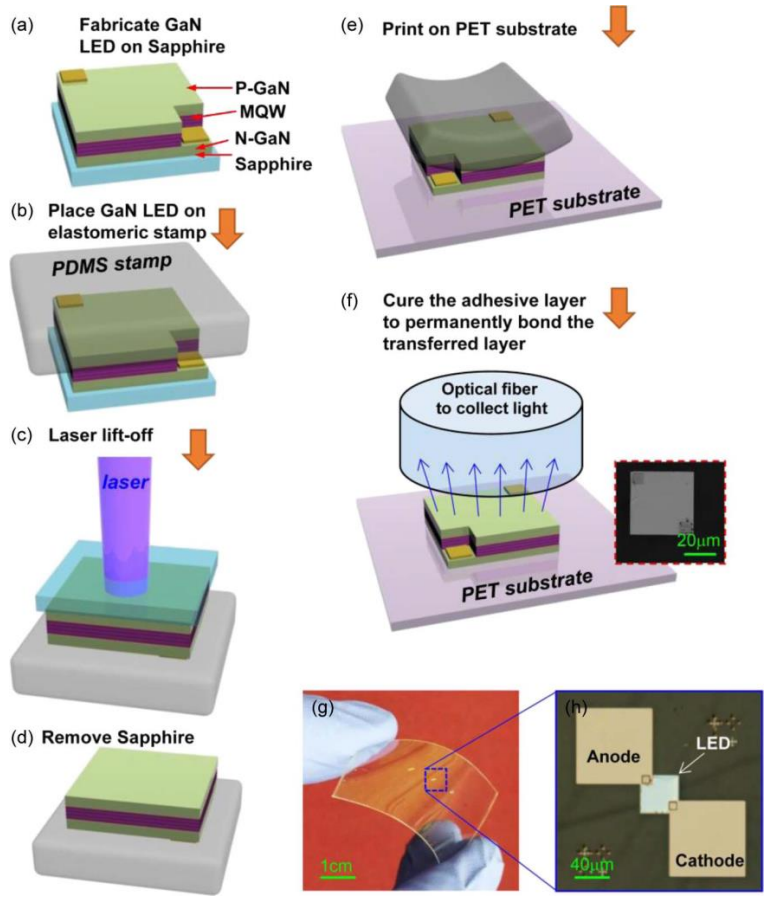

Figure 8. Schematic of the fabrication process for GaN LEDs on a PET substrate using a laser lift-off (LLO) and transfer-printing method. (**a**) Fabrication of GaN LEDs on a sapphire substrate. (**b**) Place fabricated GaN LEDs on a PDMS elastomeric stamp. (**c**) Laser lift-off from the sapphire side. (**d**) Gentle removal of the sapphire substrate. (**e**) Transfer-print GaN LED layer onto the PET substrate. (**f**) Curing of the adhesive layer to permanently bond the transfer-printed GaN LED layer. An optical fiber is placed on top of the GaN layer for light collection. (**g**) Image of the fabricated LED array on a bent PET substrate. (**h**) Zoomed-in image of an individual LED on PET (reprinted from [44]).

Both electrical and optical performances are measured and compared between LED chips on sapphire substrate and PET after the transfer-printing process. From the I-V and P-I shown in Figure 9a, the LEDs on PET substrates have a slightly smaller current and reduced optical output power under the same current. This may be attributed to the heat dissipation issue induced by PET's poorer thermal conductivity than sapphire, which did not show any melting signs during tests, however. Optical spectra under a 10-mA current for the two cases in Figure 9b show that the peak is shifted from 457 nm

to 455 nm after being transfer printed on the PET substrate. The wavelength shift is speculated to originate from the relaxed stress and band filling effects.

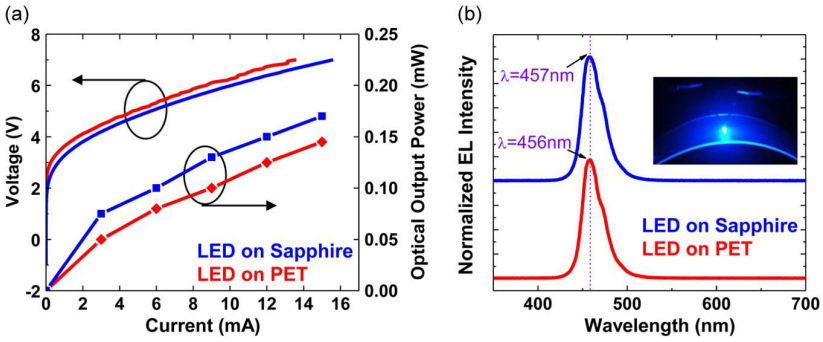

Figure 9. (**a**) Light output power-current-voltage (L-I-V) characteristics and (**b**) electroluminescent light spectra of the GaN LEDs on sapphire substrate (before laser lift-off) and PET substrates (after transfer-printing). The insert in Figure 9b shows the light emission images on a PET substrate (reprinted from [44]).

This method of using PDMS as the LLO and transfer holder provides a simplified approach to fabricate GaN LEDs on any flexible substrate without performance degradation.

3. Semiconductor Nanomembrane-Based Photodetecting Devices

To achieve a monolithically-integrated photonics circuit on a silicon platform, integrating an efficient light absorption layer onto Si has been highly desirable. Approaches developed up to now include mainly wafer boding or epitaxial growth [52]. Lattice mismatches between Si and Ge or Si and III-V will greatly degrade the material quality with large dislocations and defect density. Benefiting from being insensitive to lattice mismatch, transfer printing enjoys advantages over the two methods in terms of low cost and process simplification.

In this section, photodetecting devices based on InGaAs and Ge NMs on Si substrate are reviewed, including a multi-wavelength photodetector and a cavity-enhanced photodetector. On the other hand, flexible phototransistors and photodetectors based on InP and Si NMs on plastic substrate transfer have also been demonstrated, offering a promising route to an inorganic crystalline-based flexible photonics platform.

3.1. Multi-Color Photodetector Arrays

A multi-color photodetector covering visible and infrared (IR) has long been desired for applications, such as biophotonics, automotive cameras, imaging, free space optical communications, and so on. The conventional approach to discriminate and detect different wavelengths is by the use of filters, which is slow, bulky and requires complicated post-processing [53]. As different materials have different optical absorption spectra, membrane transfer offers a feasible way to form stacked heterogeneous material layers, thus enabling absorption and sensing targeting at different wavelengths at the same time.

A filter-free four-color photodetector based on integrated InGaAs and Si membrane over the visible and IR spectrum has been recently demonstrated [39], shown as in Figure 10. Figure 10a is the epi-layer structures of SOI wafer and InGaAs on InP substrate before the transfer process. The silicon detecting part is a vertical n-p-n-p, forming three junctions capable of detecting blue, green and red colors due to the wavelength-dependent absorption property of silicon [54], while the InGaAs section has a p-i-n single junction structure, which responds to the NIR wavelengths. Before the transfer, the InGaAs substrate is etched to define mesa and contact areas and spun with SU-8 to facilitate bonding between the Si membrane and InGaAs substrate. Then, the released Si membrane from SOI is transfer

printed onto the InP substrate with careful alignment to ensure that the two detecting parts are closely placed (Figure 10b). The thickness of Si is 6.5 μm, and the InGaAs photodetecting part is 2.56 μm. In the end, four contacts are formed for three junctions between n-p-n-p Si, and two contacts are defined on the p and n layers of InGaAs, as in Figure 10c.

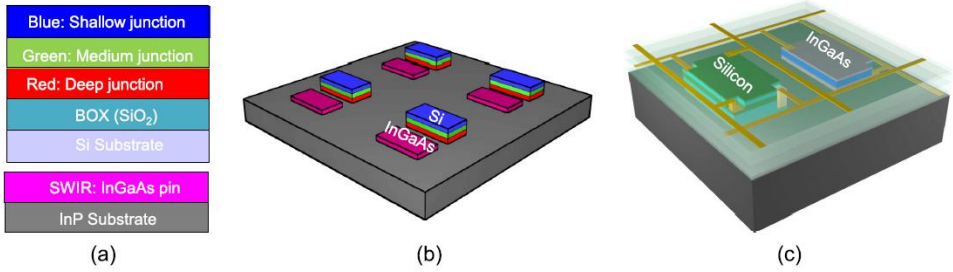

Figure 10. Schematics of the proposed crystalline-nanomembrane-based stacked multicolor multiband photodetector arrays. (**a**) Three-junction SOI wafer and the InGaAs single-junction wafer before transfer. (**b**) Si pixels transferred onto the InP substrate with precise alignment with the InGaAs pixel. (**c**) One pixel of the multicolor multiband membrane imager after device completion (reprinted from [39]).

The photocurrent responses under different incident light wavelengths and intensities are measured for the four junctions. The dark currents for all junctions are below 20 nA with a −2-V reverse bias. With light shined on the center of individual device through a lensed fiber, the responsivities for blue, green, red and IR wavelengths (4.5 nm, 532 nm, 632 nm, 980 nm and 1550 nm) are 0.09 A/W, 0.1 A/W, 0.15 A/W, 0.5 A/W and 0.8 A/W, respectively, as shown in Figure 11.

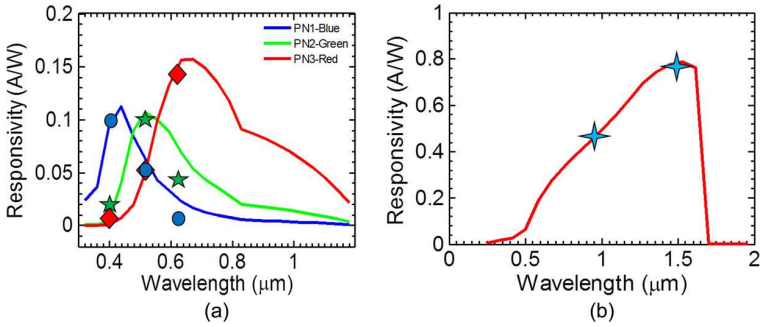

Figure 11. Simulated (solid lines) and measured (symbols) responsivity for (**a**) silicon (405 nm, 532 nm, and 632 nm) and (**b**) InGaAs (IR–980 nm, 1550 nm) (reprinted from [39]).

This work demonstrates the capability of integrating a variety of materials with different optical properties to make one photodetector unit more versatile and multi-functional, enabled by membrane transfer-printing.

3.2. Germanium Photodetector with Enhanced Quantum Efficiency

Recently, we reported resonant cavity (RC) metal-semiconductor-metal (MSM) germanium nanomembrane (Ge NM) photodetectors via stacked single-crystalline NMs by transfer printing. The Ge NM layer, released from smart-cut processed germanium-on-insulator wafer [55], was directly transferred onto the Si NM/SiO_2 distributed Bragg reflector (DBR). Therefore, a high quality Ge NM, free from misfit/threading dislocations, was obtained. The two pairs of Si NM/SiO_2 DBR were realized by repeating the single crystal Si NM transfer and partially wet oxidization process twice, as shown in Figure 12a–e. The thicknesses of SiO_2 and Si NM after oxidation were 270 and 110 nm, which are designed to have high and flat reflectivity over a 1.55-μm wavelength range. After the second

oxidation, 570 nm-thick Ge NM was transferred onto the two-pair DBR (Figure 12f). In the end, Ti/Au (10 nm/500 nm) was deposited as the anode and cathode contact metals, as shown in Figure 12g. Figure 12h shows the optical microscope image of the completed device. The width and spacing between metal electrodes are 5 and 2 μm, respectively. As a reference sample, a similar structure without DBR is fabricated, as well.

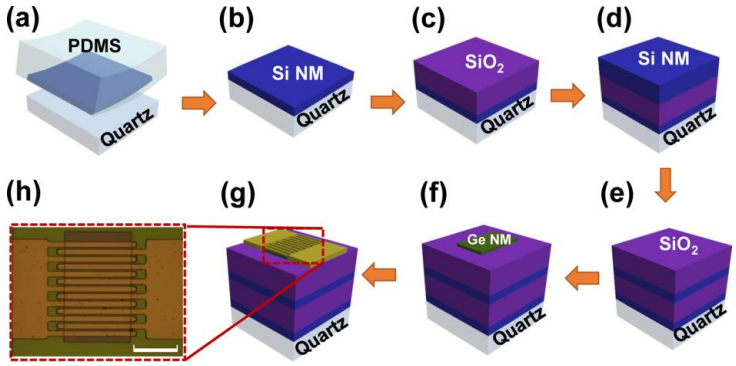

Figure 12. Schematic illustrations of the fabrication process for the resonant cavity (RC) metal-semiconductor-metal (MSM) Ge photodetectors. (**a**) Transfer Si NM with PDMS stamp. (**b**) Transferred Si NM on a quartz substrate. (**c**) Thermal oxidation after first Si NM. (**d**) Second Si NM transfer after one pair of Si/SiO_2 distributed Bragg reflector (DBR). (**e**) Second thermal oxidation. (**f**) Transferred Ge NM on two pairs of Si/SiO_2 DBR. (**g**) Complete device after Ti/Au electrode deposition and lift-off. (**h**) Optical microscope image of the RC MSM Ge photodetector. The scale bar is 50 μm (reprinted from [40]).

To compare the photo responsivity of the two type of devices, a tunable laser source is connected to a lensed fiber to couple the light into the photodetectors for the photocurrent measurement. The dark and photocurrent of the Ge photodetectors were measured, as shown in Figure 13a,b. As a result, responsivities of 0.18 and 0.09 A/W were measured at 1.55 μm under 1 V for the MSM photodetector on DBR and the one on quartz, respectively. The quantum efficiency of the RC Ge photodetector with DBR (17.3%) is about two-times larger than the one on quartz substrate (8.3%).

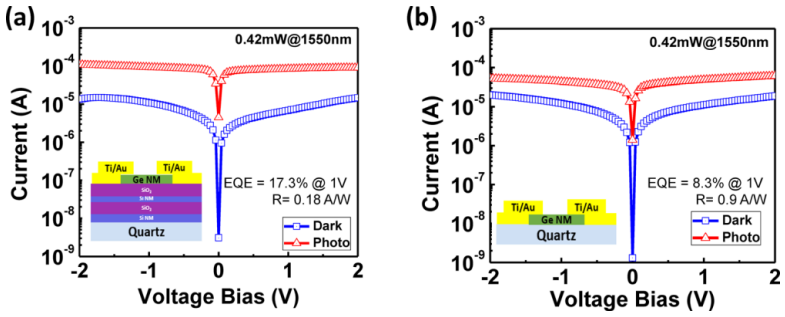

Figure 13. Measured photo/dark current of (**a**) the RC MSM Ge photodetector and (**b**) the MSM Ge photodetector on quartz substrate (reprinted from [40]).

3.3. Large-Area InP NM-Based Flexible Photodetectors

The flexible optoelectronic device has a variety of applications, such as flexible imaging, conformal photonic systems and bio-photonics. Due to the rigidity and fragility of bulk crystalline semiconductor materials, conventional flexible devices are mostly based on organic or amorphous material. The transfer printing technique allows one to combine the advantages of high performance inorganic crystalline material and mechanical flexibility of thin NM at the nanometer scale. While

for particularly fragile InP material, large-area release and transfer still is challenging, we came up with a frame-assisted membrane transfer (FAMT) process to deal with the large-area and easy-to-break membrane material. In this report, a 3 × 3 mm^2 InP NM is released from the native substrate and transferred to PET substrate. The InP structure consists of a p-i-n photodetecting diode and a InGaAs sacrificial layer underneath [56], which will be etched away during wet etching release. Before the etch and release process, two frame finger-shaped metals are deposited on top of InP NMs, acting both as the anode metal contact and mechanical support for the fragile large-area InP NM. As Figure 14a,b depicts, the InP NM is transferred on indium tin oxide (ITO)/PET substrate, and ITO functions as a transparent cathode metal.

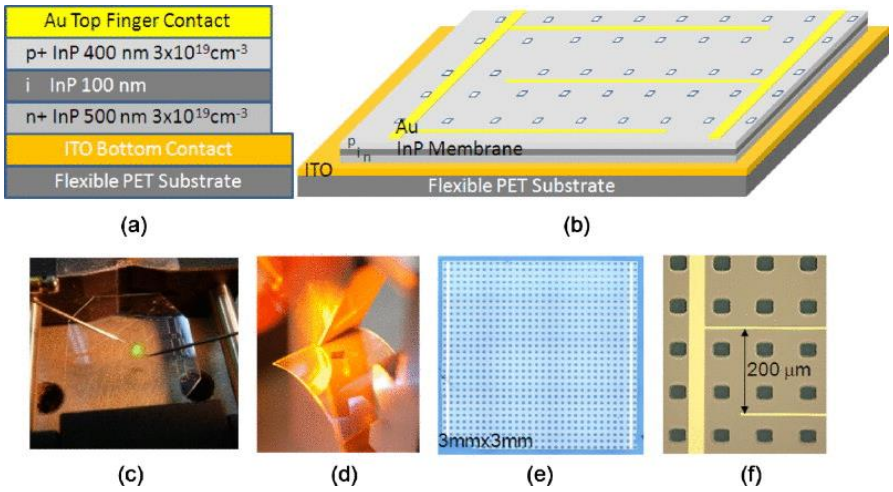

Figure 14. (**a**) Cross-sectional and (**b**) three-dimensional views of flexible InP p-i-n NM photodetecting (PD) on ITO/PET substrate. (**c**) A micrograph of fabricated flexible InP PD under test. (**d**–**f**) Zoom-in views of a fabricated large area (3 × 3 mm^2) InP PD on flexible PET substrate (reprinted from [41]).

The photodetecting performances are measured, as shown in Figure 15; the dark current is as low as 1 μA at a reverse bias of −0.5 V. Light at a 533-nm wavelength is incident on devices with different power; the photocurrent shows a nearly linear trend *versus* the light intensity (Figure 15b). The measured responsivity for 533 nm is 0.12 A/W and agrees with the theoretical calculation for the 1 μm-thick InP. To investigate the effect of bending on the device characteristics, the photo responsivities under different bending radii are compared. No obvious degradation shows with bending radii up to 38.1 mm, both for dark current and responsivity.

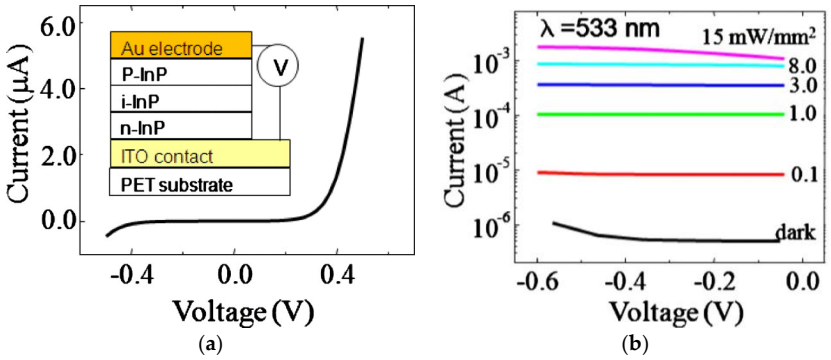

Figure 15. Measured flexible InP p-i-n PD characteristics. (**a**) Measured dark current-voltage characteristics. (**b**) Measured photocurrents at different incident optical powers for a 533-nm wavelength light source (reprinted from [41]).

3.4. Silicon NM-Based Flexible Phototransistors

Compared to the common p-n junction-based photodetectors, phototransistors have advantages in terms of responsivity and quantum efficiency. It has been reported that the metal oxide semiconductor field-effect transistors (MOSFETs) show outstanding characteristics in photosensitivity and responsivity [57]. Recently, we demonstrated a flexible phototransistor based on single crystalline silicon NMs. The Si NM is flip-transferred on flexible substrate; thus, the absorbing Si area is not limited by the channel dimension, since the light is not as blocked by the gate metal as the conventional phototransistors. On the other hand, the gate electrode beneath the detecting Si after flip transfer acts as a high reflection mirror. As a result, our proposed structure not only takes advantage of the higher photo-sensing ability, but also further improves the light absorption due to more exposure area and the half cavity enhancement effect.

As shown in Figure 16a, the device fabrication process flow starts from partially heavy n doping on a p-type-doped SOI substrate, which is later deposited with metal to form ohmic contacts for source, drain and gate, respectively (Figure 16c). Before the metal e-beam evaporation, a typical NM release process is employed to make the Si NM ready to be picked up by PET substrate with an adhesive layer (Figure 16d). Furthermore, an anti-reflection layer (SU-8 2002) is coated on top of flipped Si NM to improve the light absorption efficiency. The finished phototransistor on flexible PET substrate is shown in the microscopic image as Figure 16f.

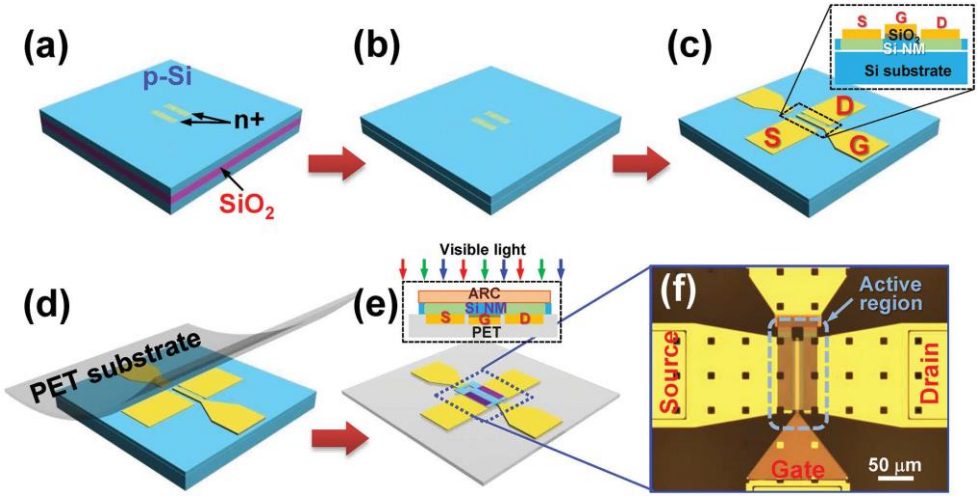

Figure 16. The schematic illustration of the device fabrication process flow. (**a**) Beginning with forming n+ regions by ion implantation of source/drain regions to achieve an ohmic contact. (**b**) Releasing Si NM by selective etching of a buried oxide layer. (**c**) Metallization by e-beam evaporation to deposit source/drain electrodes and a stack of gate/gate dielectric. (**d**) Transfer printing fully-fabricated devices to adhesive layer-coated PET substrate. (**e**) Spin-coating a protection layer on top of the surface. (**f**) Microscopic image of a finished flexible phototransistor. Insets in (c,e) depict the cross-sectional view of device (reprinted from [25]).

The gate channel is 50 μm wide and 2 μm long, and the thickness of Si NM is 270 nm. Dark current and photocurrent with red (632 nm), green (532 nm) and blue (473 nm) laser illuminations are measured under two scenarios; one is under low gate bias to obtain a high photo-to-dark current ratio, and the other is under relatively high gate voltage to achieve high responsivity. For the first operation condition, the phototransistor yields up to a 10^5 photo-to-dark ratio under 0.5 V for V_{GS} and 0.05 V for V_{DS}, while the responsivity only shows 0.04 A/W due to the very thin Si NM used for the absorption gating layer. As gate bias increased to 1 V, the photo-to-dark ratio drops to 11, but the drain current increase significantly, as shown in Figure 17b. The responsivity at a voltage bias of V_{GS} = 1 V and V_{DS} = 3 V is calculated to be 51, 41 and 18 A/W under red, green and blue incident light, respectively.

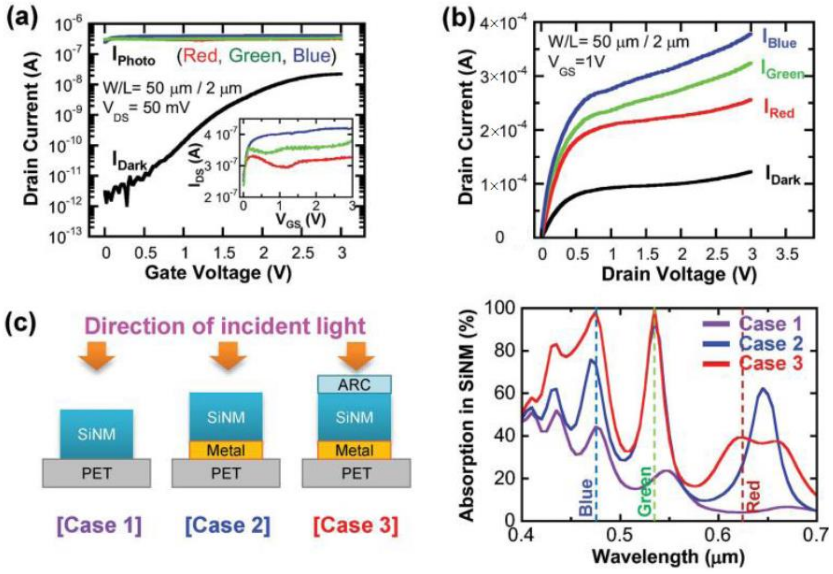

Figure 17. (**a**) Drain current-gate voltage characteristics (I_{DS}-V_{GS}) at V_{DS} = 0 V. The inset shows the magnified plot of photo currents. (**b**) Drain current-drain voltage characteristics (I_{DS}-V_{GS}) under dark and illumination with various light sources (red, green and blue) onto flexible phototransistors. The I_{DS}-V_{GS} curve under V_{GS} = 1 V for the photo-to-dark current ratio shows as high as $\approx 1 \times 10^5$. (**c**) (Left) Three layer structures used to simulate the light absorption of Si NM, (right) and their corresponding simulated absorption of Si NM: (i) without any layers; (ii) with the metal reflector underneath the Si NM; (iii) with the metal reflector underneath the Si NM and SU-8 ARC layer on the top of Si NM, respectively. The dashed line denotes blue (473 nm), green (532 nm) and red (632 nm) wavelengths (reprinted from [25]).

To investigate the effects of metal reflector and anti-reflection coating on the light absorption enhancement, three cases shown as in Figure 17c are simulated with regard to the optical properties in the 400–700-nm visible wavelength range. The simulation shows that the average absorption percentage in Si NM with the reflector and anti-reflection layer is increased more than twice from 20.2%–48%, compared to Si NM directly on PET substrate.

Devices with different Si NM channel active area dimensions are also fabricated and measured to explore the influences; the larger width/length ratio shows higher photo responsivity. Under bending at curvature radii of 15 mm, the device is proven to be stable in terms of responsivity, which provides great promises for flexible photodetecting applications.

3.5. Flexible Photodetecting P-N Diode between Pentacene and Si NM

Besides stack between various inorganic semiconductor materials, the heterogeneous p-n junction between organic and inorganic material has also been demonstrated by transfer printing. It is reported in [42] that an n-doped single crystal Si NM, which is transfer printed on a plastic substrate, forms a heterogeneous p-n diode with a p-doped pentacene. Figure 18a is the microscopic picture of the Si NM with a hexagonal meshed pattern on PET substrate, partly covered by Au metal. The pentacene is on the right side of the Si NM, as shown in Figure 18b. The vertical p-n diode structure can be clearly seen in the inset schematic drawing. The scanning electron microscopy (SEM) image of the device is shown in Figure 18c, and atomic force microscopy (AFM) shows the pentacene surface with an average grain size of 180 nm.

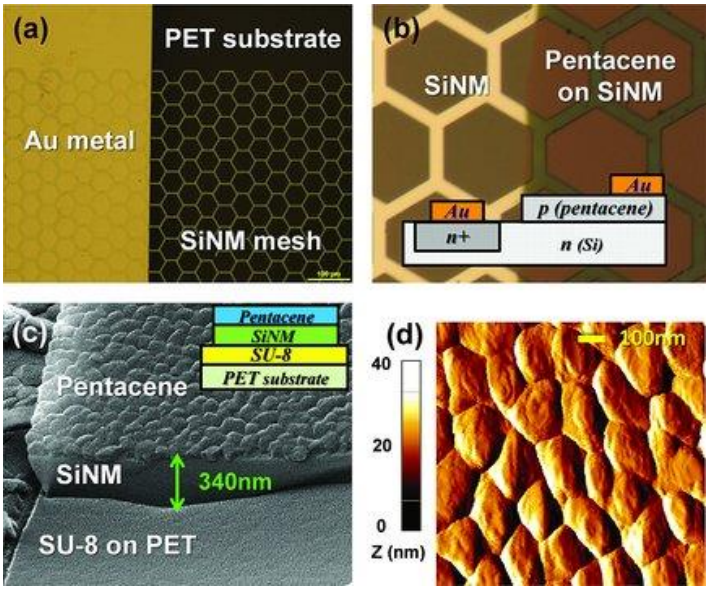

Figure 18. (**a**) Microscopic image of transferred Si NM grid on PET substrate. (**b**) Microscopic images of Si NM (left)/pentacene (right) heterojunction. The inset shows the cross-section of the heterostructure. (**c**) SEM image of Si NM and deposited pentacene layer sitting on SU-8-coated PET substrate. The inset shows the detailed layer structure. (**d**) AFM image of deposited pentacene on Si NM. The average pentacene grain size is 180 nm (reprinted from [42]).

The I-V characteristics of the Si-pentacene p-n diode are measured, showing a good rectifying behavior with ideality factor n = 1.89. The relatively high series resistance is due to the low hole mobility for pentacene and the possible presence of native oxide. The photodetecting characteristics with different incident light wavelengths are also measured, and it shows photo responsivity of 0.7 A/W for 532-nm illumination. The external quantum efficiency is calculated to be 21.9% at a 632-nm laser illumination, which is the highest over 473–905 nm. The effects of mechanical flexibility on device performances are also examined. Figure 19 shows the I-V characteristics of the Si-pentacene diode under different convex bending radii from 77.5 mm down to 15 mm, which indicates not much degradation. The photocurrent *versus* bending strain is depicted, as well, in Figure 19b, showing that the external quantum efficiency increases to 25.1% from 21.9% under a bending strain of 1.08%.

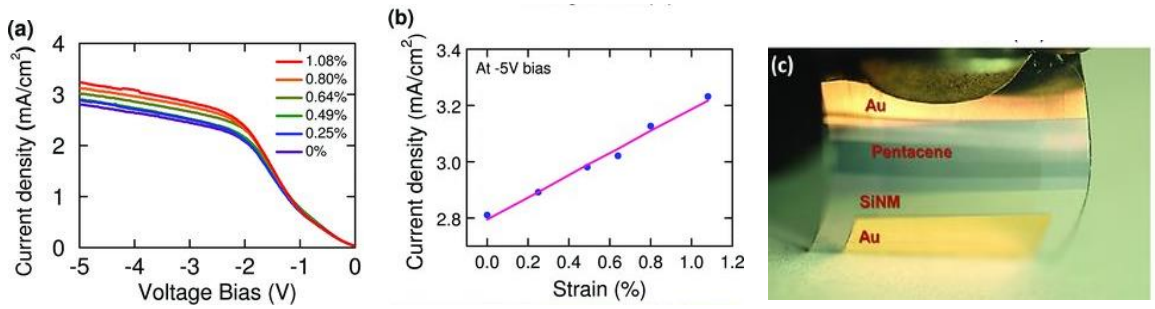

Figure 19. Characterizations Si NM-pentacene diode under mechanical bending. (**a**) Measured photocurrent of the diode under different bending strains. (**b**) Plot of photocurrent change as a function of strain. (**c**) An optical image of the diode under bending (reprinted from [42]).

To investigate the cause for this improved photocurrent and external quantum efficiency, the Raman confocal microscope is used to reflect the strain effect of the two materials. It is found under tensile strain that the three vibration mode peaks of pentacene have shifted under the bending

condition. According to the study that the Raman peak shift is related to the mobility improvement of pentacene [58,59], this photocurrent enhancement under the bending condition could be explained by the mobility improvement, given that tensile strain on the crystal lattice could increase the carriers' mobility of Si NM, as well [6,60].

Due to thickness of only 340 nm and meshed hexagonal pattern, the Si NM and pentacene heterojunction structure on PET is highly transparent for visible light, as Figure 8c shows. Thus, an optically-transparent, photosensitive and flexible heterogeneous p-n diode between organic pentacene and inorganic Si NM is demonstrated based on transfer printing, extending the boundary of the transfer printing technique to even broader material choices.

4. Conclusions and Outlooks

In summary, transfer printing has provided a practical approach to hybrid integration of a large variety of materials with different electrical and optical characteristics to achieve versatile and high performance optoelectronic systems. The III-V group gain material and photon sensing Ge on Si substrate by transfer printing approach offers tremendous application potentials on a CMOS-compatible silicon photonics platform. Moreover, the bendable inorganic single-crystal semiconductor NM has also been enabled, which makes possible the integrated optoelectronics in flexibility-required applications, such as wearable devices and second skin. At the same time, the heterogeneous p-n diode formed by transfer printing with good electronic behavior also indicates that this technique is not limited to the applications just in mechanical bonding between different materials, but also provides infinite possibilities to form arbitrary heterojunctions with various combinations of materials.

Acknowledgments: The work was supported by AFOSR under grants: FA9550-11-C-0026, FA9550-09-1-0482, FA9550-09-C-0200, FA9550-08-1-0337, by ARO under Grant W911NF-09-1-0505 and by NSF under Grant ECCS-1308520.

Conflicts of Interest: The authors declare no conflict of interest.

References

1. Rogers, J.A.; Lagally, M.G.; Nuzzo, R.G. Synthesis, assembly and applications of semiconductor nanomembranes. *Nature* **2011**, *477*, 45–53. [CrossRef] [PubMed]
2. Hwang, S.W.; Tao, H.; Kim, D.H.; Cheng, H.; Song, J.K.; Rill, E.; Brenckle, M.A.; Panilaitis, B.; Won, S.M.; Kim, Y.S.; *et al.* A physically transient form of silicon electronics. *Science* **2012**, *337*, 1640–1644. [CrossRef] [PubMed]
3. Schmidt, O.G.; Eberl, K. Nanotechnology: Thin solid films roll up into nanotubes. *Nature* **2001**, *410*, 168. [CrossRef] [PubMed]
4. Trotta, R.; Atkinson, P.; Plumhof, J.; Zallo, E.; Rezaev, R.; Kumar, S.; Baunack, S.; Schröter, J.; Rastelli, A.; Schmidt, O. Nanomembrane quantum light emitting diodes integrated onto piezoelectric actuators. *Adv. Mater.* **2012**, *24*, 2668–2672. [CrossRef] [PubMed]
5. Li, X. Self-rolled-up microtube ring resonators: A review of geometrical and resonant properties. *Adv. Opt. Photonic* **2011**, *3*, 366–387. [CrossRef]
6. Scott, S.A.; Lagally, M.G. Elastically strain-sharing nanomembranes: Flexible and transferable strained silicon and silicon-germanium alloys. *J. Phys. D Appl. Phys.* **2007**, *40*, R75–R92. [CrossRef]
7. Yuan, H.C.; Ma, Z.; Roberts, M.M.; Savage, D.E.; Lagally, M.G. High-speed strained-single-crystal-silicon thin-film transistors on flexible polymers. *J. Appl. Phys.* **2006**, *100*. [CrossRef]
8. Sun, L.; Qin, G.; Seo, J.H.; Celler, G.K.; Zhou, W.; Ma, Z. 12 GHz thin film transistors on transferrable silicon nanomembranes for high performance flexible electronics (cover story). *Small* **2010**, *6*, 2553–2557. [CrossRef] [PubMed]
9. Zhang, K.; Seo, J.H.; Zhou, W.; Ma, Z. Fast flexible electronics using transferrable silicon nanomembranes (topical review). *J. Phys. D Appl. Phys.* **2012**, *45*. [CrossRef]

10. Zhou, W.; Ma, Z.; Yang, H.; Qiang, Z.; Qin, G.; Pang, H.; Chen, L.; Yang, W.; Chuwongin, S.; Zhao, D. Flexible photonic-crystal fano filters based on transferred semiconductor nanomembranes. *J. Phys. D Appl. Phys.* **2009**, *42*. [CrossRef]
11. Zhou, W.; Ma, Z.; Yang, H.; Chen, L.; Yang, W.; Qiang, Z.; Qin, G.; Pang, H.; Chuwongin, S.; Zhao, D. Semiconductor nanomembranes for stacked and flexible photonics. In Proceedings of the International Society for Optics and Photonics, San Francisco, CA, USA, 23 January 2010; p. 76060U.
12. Yang, H.; Zhao, D.; Chuwongin, S.; Seo, J.H.; Yang, W.; Shuai, Y.; Berggren, J.; Hammar, M.; Ma, Z.; Zhou, W. Transfer-printed stacked nanomembrane lasers on silicon. *Nat. Photonic* **2012**, *6*, 615–620. [CrossRef]
13. Zhou, H.; Seo, J.-H.; Paskiewicz, D.M.; Zhu, Y.; Celler, G.K.; Voyles, P.M.; Zhou, W.; Lagally, M.G.; Ma, Z. Fast flexible electronics with strained silicon nanomembranes. *Sci. Rep.* **2013**, *3*. [CrossRef] [PubMed]
14. Meitl, M.A.; Zhu, Z.T.; Kumar, V.; Lee, K.J.; Feng, X.; Huang, Y.Y.; Adesida, I.; Nuzzo, R.G.; Rogers, J.A. Transfer printing by kinetic control of adhesion to an elastomeric stamp. *Nat. Mater.* **2006**, *5*, 33–38. [CrossRef]
15. Harazim, S.M.; Quinones, V.A.B.; Kiravittaya, S.; Sanchez, S.; Schmidt, O. Lab-in-a-tube: On-chip integration of glass Optofluidic Ring Resonators for label-free Sensing Applications. *Lab Chip* **2012**, *12*, 2649–2655. [CrossRef] [PubMed]
16. Song, Y.M.; Xie, Y.; Malyarchuk, V.; Xiao, J.; Jung, I.; Choi, K.-J.; Liu, Z.; Park, H.; Lu, C.; Kim, R.-H. Digital cameras with designs inspired by the arthropod eye. *Nature* **2013**, *497*, 95–99. [CrossRef] [PubMed]
17. Zhou, W.; Ma, Z. Breakthroughs in nanomembranes and nanomembrane lasers. *IEEE Photonic J.* **2013**, *5*. [CrossRef]
18. Zhou, W.; Zhao, D.; Shuai, Y.-C.; Yang, H.; Chuwongin, S.; Chadha, A.; Seo, J.-H.; Wang, K.X.; Liu, V.; Ma, Z. Progress in 2D photonic crystal Fano resonance photonics. *Prog. Quantum Electron.* **2014**, *38*, 1–74. [CrossRef]
19. Hu, J.; Li, L.; Lin, H.; Zhang, P.; Zhou, W.; Ma, Z. Flexible integrated photonics: Where materials, mechanics and optics meet (invited). *Opt. Mater. Express* **2013**, *3*, 1313–1331. [CrossRef]
20. Roberts, M.M.; Klein, L.J.; Savage, D.E.; Slinker, K.A.; Friesen, M.; Celler, G.; Eriksson, M.A.; Lagally, M.G. Elastically relaxed free-standing strained-silicon nanomembranes. *Nat. Mater.* **2006**, *5*, 388–393. [CrossRef] [PubMed]
21. Rogers, J.A.; Someya, T.; Huang, Y. Materials and mechanics for stretchable electronics. *Science* **2010**, *327*, 1603–1607. [CrossRef] [PubMed]
22. Janglin, C.; Liu, C.T. Technology advances in flexible displays and substrates. *IEEE Access* **2013**, *1*, 150–158. [CrossRef]
23. Ko, H.; Takei, K.; Kapadia, R.; Chuang, S.; Fang, H.; Leu, P.W.; Ganapathi, K.; Plis, E.; Kim, H.S.; Chen, S.-Y. Ultrathin compound semiconductor on insulator layers for high-performance nanoscale transistors. *Nature* **2010**, *468*, 286–289. [CrossRef] [PubMed]
24. Chen, Y.; Li, H.; Li, M. Flexible and tunable silicon photonic circuits on plastic substrates. *Sci. Rep.* **2012**, *2*. [CrossRef] [PubMed]
25. Seo, J.H.; Zhang, K.; Kim, M.; Zhao, D.; Yang, H.; Zhou, W.; Ma, Z. Flexible phototransistors based on single-crystalline silicon nanomembranes. *Adv. Opt. Mater.* **2015**, *4*. [CrossRef]
26. Seo, J.-H.; Zhang, Y.; Yuan, H.-C.; Wang, Y.; Zhou, W.; Ma, J.; Ma, Z.; Qin, G. Investigation of various mechanical bending strains on characteristics of flexible monocrystalline silicon nanomembrane diodes on a plastic substrate. *Microelectron. Eng.* **2013**, *110*, 40–43. [CrossRef]
27. Gao, L.; Zhang, Y.; Malyarchuk, V.; Jia, L.; Jang, K.-I.; Webb, R.C.; Fu, H.; Shi, Y.; Zhou, G.; Shi, L. Epidermal photonic devices for quantitative imaging of temperature and thermal transport characteristics of the skin. *Nat. Commun.* **2014**, *5*. [CrossRef] [PubMed]
28. Huang, C.C.; Wu, X.; Liu, H.; Aldalali, B.; Rogers, J.A.; Jiang, H. Large-field-of-view wide-spectrum artificial reflecting superposition compound eyes. *Small* **2014**, *10*, 3050–3057. [CrossRef] [PubMed]
29. Xu, X.; Subbaraman, H.; Kwong, D.; Hosseini, A.; Zhang, Y.; Chen, R.T. Large area silicon nanomembrane photonic devices on unconventional substrates. *IEEE Photonic Technol. Lett.* **2013**, *25*, 1601–1604. [CrossRef]
30. Zhao, D.; Liu, S.-C.; Yang, H.; Ma, Z.; Carl, R.-H.; Mattias, H.; Zhou, W. Printed Large-Area Single-Mode Photonic Crystal Bandedge Surface-Emitting Lasers on Silicon. *Sci. Rep.* **2016**, *6*, 18860. [CrossRef] [PubMed]
31. Yang, H.; Zhao, D.; Liu, S.; Liu, Y.; Seo, J.-H.; Ma, Z.; Zhou, W. Transfer Printed Nanomembranes for Heterogeneously Integrated Membrane Photonics. *Photonics* **2015**, *2*, 1081–1100. [CrossRef]

32. Xu, X.; Subbaraman, H.; Chakravarty, S.; Hosseini, A.; Lin, C.-Y.; Kwong, D.; Chen, R.T. Stamp printing of silicon-nanomembrane-based photonic devices onto flexible substrates with a suspended configuration. *Opt. Lett.* **2012**, *37*, 1020–1022. [CrossRef] [PubMed]
33. Xu, X.; Subbaraman, H.; Chakravarty, S.; Hosseini, A.; Covey, J.; Yu, Y.; Chen, R.T. Flexible single-crystal silicon nanomembrane photonic crystal cavity. *ACS Nano* **2014**, *8*, 12265–12271. [CrossRef] [PubMed]
34. Yang, H.; Zhao, D.; Seo, J.-H.; Chuwongin, S.; Kim, S.; Rogers, J.A.; Ma, Z.; Zhou, W. Broadband membrane reflectors on glass. *IEEE Photonic Technol. Lett.* **2012**, *24*, 476–478. [CrossRef]
35. Yang, H.; Pang, H.; Qiang, Z.; Ma, Z.; Zhou, W. Surface-normal fano filters based on transferred silicon nanomembranes on glass substrates. *Electron. Lett.* **2008**, *44*, 858–859. [CrossRef]
36. Qiang, Z.; Yang, H.; Chen, L.; Pang, H.; Ma, Z.; Zhou, W. Fano filters based on transferred silicon nanomembranes on unconventional substrates. *IEEE Photonic Technol. Lett.* **2013**, *25*, 1601–1604.
37. Jung, Y.; Chang, T.-H.; Zhang, H.; Yao, C.; Zheng, Q.; Yang, V.; Mi, H.; Kim, M.; Cho, S.-J.; Park, D.-W.; *et al.* High-performance green flexible electronics based on biodegradable cellulose nanofibril paper. *Nat. Commun.* **2015**, *6*, 7170. [CrossRef] [PubMed]
38. Justice, J.; Bower, C.; Meitl, M.; Mooney, M.; Gubbins, M.; Corbett, B. Wafer-scale integration of group III-V lasers on silicon using transfer printing of epitaxial layers. *Nat. Photonic* **2012**, *6*, 610–614. [CrossRef]
39. Menon, L.; Yang, H.; Cho, S.-J.; Mikael, S.; Ma, Z.; Carl, R.-H.; Mattias, H.; Zhou, W. Heterogeneously Integrated InGaAs and Si Membrane Four-Color Photodetector Arrays. *IEEE Photonics J.* **2016**, *8*, 1–7. [CrossRef]
40. Cho, M.; Seo, J.-H.; Kim, M.; Lee, J.; Liu, D.; Zhou, W.; Yu, Z.; Ma, Z. Resonant cavity germanium photodetector via stacked single-crystalline nanomembranes. *JVSTB* **2016**, *34*. [CrossRef]
41. Yang, W.; Yang, H.; Qin, G.; Ma, Z.; Berggren, J.; Hammar, M.; Soref, R.; Zhou, W. Large-area InP-based crystalline nanomembrane flexible photodetectors. *Appl. Phys. Lett.* **2010**, *96*. [CrossRef]
42. Seo, J.-H.; Oh, T.-Y.; Park, J.; Zhou, W.; Ju, B.-K.; Ma, Z. A Multifunction Heterojunction Formed between Pentacene and a Single-Crystal Silicon Nanomembrane. *Adv. Funct. Mater.* **2013**, *23*, 3398–3403. [CrossRef]
43. Xia, Z.; Song, H.; Kim, M.; Zhou, M.; Chang, T.; Liu, D.; Xiong, K.; Yu, Z.; Ma, Z.; Gan, Q. Photodetecting MOSFET based on ultrathin single-crystal germanium nanomembrane. In Proceedings of Conference on Lasers and Electro-Optics: Science and Innovations 2016, San Jose, CA, USA, 5–10 June 2016.
44. Seo, J.-H.; Li, J.; Lee, J.; Lin, J.; Jiang, H.; Ma, Z. A simplified method of making flexible blue LEDs on a plastic substrate. *IEEE Photonic* **2015**, *7*. [CrossRef]
45. Chen, R.; Tran, T.-T.D.; Ng, K.; Ko, W.; Chuang, L.; Sedgwick, F.; Chang-Hasnain, C. Nanolasers grown on silicon. *Nat. Photonic* **2011**, *5*, 170–175. [CrossRef]
46. Fang, A.W.; Cohen, O.; Jones, R.; Paniccia, M.J.; Bowers, J.E. Design and fabrication of optically pumped hybrid silicon-AlGaInAs evanescent lasers. *IEEE J. Sel. Top. Quantum Electron.* **2006**, *12*, 1657–1663.
47. Fang, A.W.; Park, H.; Cohen, O.; Jones, R.; Paniccia, M.J.; Bowers, J.E. Electrically pumped hybrid AlGaInAs-silicon evanescent laser. *Opt. Express* **2006**, *14*, 9203–9210. [CrossRef] [PubMed]
48. Vecchi, G.; Raineri, F.; Sagnes, I.; Yacomotti, A.; Monnier, P.; Karle, T.J.; Lee, K.-H.; Braive, R.; Gratiet, L.; Guilet, S.; *et al.* Continuous-wave operation of photonic band-edge laser near 1.55 μm on silicon wafer. *Opt. Express* **2007**, *15*, 7551–7556. [CrossRef] [PubMed]
49. Hirose, K.; Liang, Y.; Kurosak, Y.; Watanabe, A.; Sugiyama, T.; Noda, S. Watt-class high-power, high-beam-quality photonic-crystal lasers. *Nat. Photonic* **2014**, *8*, 406–411. [CrossRef]
50. Noda, S.; Yokoyama, M.; Imada, M.; Chutinan, A.; Mochizuki, M. Polarization mode control of two-dimensional photonic crystal laser by unit cell structure design. *Science* **2001**, *293*, 1123–1125. [CrossRef] [PubMed]
51. Miyai, E.; Sakai, K.; Okano, T.; Kunishi, W.; Ohnishi, D.; Noda, S. Photonics: Lasers producing tailored beams. *Nature* **2006**, *441*, 946–946. [CrossRef] [PubMed]
52. Dosunmu, O.I.; Cannon, D.D.; Emsley, M.K.; Ghyselen, B.; Liu, J.; Kimerling, L.C.; Unlu, M. Resonant Cavity Enhanced Ge Photodetectors for 1550 nm Operation on Reflecting Si Substrates. *IEEE J. Sel. Top. Quantum Electron.* **2004**, *10*, 694–701. [CrossRef]
53. Tsagaris, V.; Anastassopoulos, V. Fusion of visible and infrared imagery for night color vision. *Displays* **2005**, *26*, 191–196. [CrossRef]
54. Menon, L.; Yang, H.; Cho, S.; Mikael, S.; Ma, Z.; Zhou, W. Transferred flexible three-color silicon membrane photodetector arrays. *IEEE Photonic J.* **2015**, *7*, 1–6. [CrossRef]

55. Michel, B.; Bernard, A.; Andre-Jacques, A.-H. Smart-Cut: A New Silicon on Insulator Material Technology Based on Hydrogen Implantation and Wafer Bonding. *Jpn. J. Appl. Phys.* **1997**, *36*, 1636–1641.
56. Chen, L.; Qiang, Z.; Yang, H.; Pang, H.; Ma, Z.; Zhou, W. Polarization and angular dependent transmissions on transferred nanomembrane Fano filters. *Opt. Express* **2009**, *17*, 8396–8406. [CrossRef] [PubMed]
57. Hamilton, M.C.; Martin, S.; Kanicki, J. Thin-Film Organic Polymer Phototransistors. *IEEE Trans. Electron. Devices* **2004**, *51*, 877–885. [CrossRef]
58. Cheng, H.L.; Liang, X.W.; Chou, W.Y.; Mai, Y.S.; Yang, C.Y.; Chang, L.R.; Tang, F.C. Raman spectroscopy applied to reveal polycrystalline grain structures and carrier transport properties of organic semiconductor films: Application to pentacene-based organic transistors. *Org. Electron.* **2009**, *10*, 289–298. [CrossRef]
59. Cheng, H.L.; Chou, W.Y.; Kuo, C.W.; Tang, F.C.; Wang, Y.W. Electric field-induced structural changes in pentacene-based organic thin-film transistors studied by *in situ* micro-Raman spectroscopy. *Appl. Phys. Lett.* **2006**, *88*. [CrossRef]
60. Peng, C.-Y.; Huang, C.-F.; Fu, Y.-C.; Yang, Y.-H.; Lai, C.-Y.; Chang, S.-T.; Liu, C.W. Comprehensive study of the Raman shifts of strained silicon and germanium. *J. Appl. Phys.* **2009**, *105*. [CrossRef]